PAPER

Carbon dioxide activation by discandium dioxide cations in the gas phase: a combined investigation of infrared photodissociation spectroscopy and DFT calculations†

Pengcheng Liu,‡[ab] Jia Han,‡[c] Yan Chen,[d] Shun Lu,[d] Quyan Su,[d] Xiaoguo Zhou [iD] *[cd] and Weijun Zhang*[a]

We present a combined computational and experimental study of CO_2 activation at the $Sc_2O_2^+$ metal oxide ion center in the gas phase. Density functional theory calculations on the structures of $[Sc_2O_2(CO_2)_n]^+$ (n = 1–4) ion–molecule complexes reveal a typical end-on binding motif as well as bidentate and tridentate carbonate-containing configurations. As the number of attached CO_2 molecules increases, activated forms tend to dominate the isomeric populations. Distortion energies are unveiled to account for the conversion barriers from molecularly bound isomers to carbonate structures, and show a monotonically decreasing trend with successive CO_2 ligand addition. The infrared photodissociation spectra of target ion–molecule complexes were recorded in the 2100–2500 cm^{-1} frequency region and interpreted by comparison with simulated IR spectra of low-lying isomers representing distinct configurations, demonstrating a high possibility of carbonate structure formation in current experiments.

1. Introduction

The increasing atmospheric levels of carbon dioxide (CO_2), one of the primary greenhouse gases, have raised significant concerns. Severe environmental issues such as global warming and ocean acidification resulting from CO_2 emissions from fossil fuel combustion pose a growing threat to life on earth.[1–3] To this end, extensive studies have been focused on developing catalysts and sorbents to effectively reduce the concentration of CO_2.[4–7] The conversion of this abundantly available carbon source into environmentally benign or industrially valuable products also opens up novel opportunities to meet the growing energy demands.[8–11] However, its high ionization potential, negative electron affinity and strong C=O double bond under

[a] Anhui Institute of Optics and Fine Mechanics, Hefei Institutes of Physical Science, Chinese Academy of Sciences, Hefei 230031, China. E-mail: wjzhang@aiofm.ac.cn
[b] Science Island Branch, Graduate School, University of Science and Technology of China, Hefei 230026, China
[c] Hefei National Laboratory for Physical Sciences at the Microscale, University of Science and Technology of China, Hefei 230026, China.
E-mail: xzhou@ustc.edu.cn
[d] Department of Chemical Physics, University of Science and Technology of China, Hefei 230026, China
† Electronic supplementary information (ESI) available. See DOI: https://doi.org/10.1039/d3cp04995g
‡ These authors contributed equally to this work.

ambient conditions constitute one of the ultimate challenges for activating CO_2.[12,13] Notably, reducing CO_2 by accepting electron density when coordinated as a ligand offers a promising avenue to achieve its chemical conversion into commercially important feedstocks.[12,14,15]

Transition metal oxides, known for their capabilities of CO_2 adsorption and activation, have attracted considerable attention in the development of efficient catalysts for the sequestration and transformation of CO_2 in recent years.[16–19] Heterogeneous photocatalytic reduction of CO_2 to value-added chemicals including formic acid, formaldehyde, methanol as well as basic hydrocarbons on TiO_2, ZnO and other metal oxide semiconductors has been intensively reported.[15,20,21] The capture of CO_2 on transition metal oxide surfaces majorly involves chemisorption, leading to the formation of carbonate species or pure physisorption in nonactivated processes, where CO_2 binds to metal sites through electrostatic interactions.[22] It is complicated to precisely determine specific binding motifs for CO_2 molecules interacting with transition metal oxide surfaces considering the perturbing effects of morphology, defect density or surface atoms in the condensed phase. Therefore, further investigations into the fundamental interactions between CO_2 and transition metal oxides are urgently needed to deepen our understanding of the mechanistic aspects of CO_2 adsorption and activation.

Gas-phase studies of isolated and well-defined clusters as prototypical systems for modelling chemical reactions provide

This journal is © the Owner Societies 2023

Phys. Chem. Chem. Phys., 2023, **25**, 32853–32862 | 32853

rich opportunities to probe structural details and uncover intrinsic activation mechanisms at the molecular level.[23–31] Vibrational spectroscopic measurements of NiO_2^+ and $Mn_xO_y^+$ (x = 2–5) reacting with CO_2 molecules revealed little evidence of activation.[32,33] Jiang and co-workers found the conversion from molecular coordination motifs to carbonate-containing structures in the infrared photodissociation spectroscopic studies of third-row transition metal monoxides ScO^+ and YO^+ upon coordination of more than four CO_2 ligands.[34,35] Mackenzie *et al.* reported the possible formation of a carbonate moiety in the $[NiO_2(CO_2)_n]^+$ and $[TaO_2(CO_2)_n]^+$ ion–molecule complexes using the messenger tagging technique, and further identified unambiguous indications of a carbonate radical anion in the subsequent infrared action spectroscopic study of $[HoO(CO_2)_n]^+$.[36,37] The reactivity of TaO_3^+ cations towards CO_2 molecules was examined by similar methods and only end-on configurations driven by noncovalent interactions were characterized.[38] A distinctive bidentate $M[\eta^2\text{-(O,O)C}]$ motif was observed in the $[ZrO(CO_2)_{n\geq4}]^+$ complexes, indicating substantial activation of CO_2.[39] In particular, anionic metal oxide species present higher possibilities of various activation modes in the presence of an excess electron.[40] Carbonates with monodentate, bidentate or tridentate binding motifs were identified as dominant contributing structures in the infrared studies of CoO^-, NiO^-, TiO_x^- (x = 1–3) and $Ti_3O_6^-$ anions complexed with CO_2 ligands.[41–44] Quantum chemical calculations have been employed to simulate the adsorption of CO_2 on group IV metal oxide clusters including neutral and anionic $(MO_2)_n$ (M = Ti, Zr, and Hf) clusters, with chemisorption being more favored; whereas group VI $(MO_3)_n$ (M = Cr, Mo, W) were predicted to have weak binding with CO_2.[45,46]

Herein, we report a combined theoretical and infrared photodissociation spectroscopic study on $[Sc_2O_2(CO_2)_n]^+$ (n = 1–4) ion–molecule complexes. Using high-level quantum chemical calculations, both nonactivated interactions where CO_2 weakly coordinates to the metal end *via* one of its oxygen atoms, and activated forms with bidentate and tridentate carbonate core structures are located. The stepwise solvation has a pronounced effect on the energetics of different structural motifs and corresponding conversion barrier heights. Analyses of the recorded infrared photodissociation spectra imply the formation of carbonate structures under current experimental conditions, providing mechanistic insights into the adsorption and activation of CO_2 molecules by scandium oxides.

2. Experimental and computational methods

The infrared photodissociation spectra of $[Sc_2O_2(CO_2)_n]^+$ (n = 1–4) complex ions were obtained using a collinear tandem time-of-flight (TOF) mass spectrometer equipped with a laser vaporization ion source as illustrated in Fig. S1 (ESI†). In brief, the target ion–molecule complexes were generated by the reactions of the vaporized species with CO_2 molecules during laser ablation of a scandium disk with a Nd:YAG laser operating at 532 nm in the presence of helium carrier gas seeded with 10% CO_2. The backing pressure of the reaction gas was adjusted in the range of 4.0–6.0 × 10^5 Pa to obtain desired ion intensities and size distributions. After free expansion, the ions of interest were mass-selected and decelerated into the extraction region of a second-stage TOF mass spectrometer and then intersected using a tunable IR laser. Typical infrared photodissociation spectra were recorded by monitoring the dissociation yield of the fragment ions as a function of IR photon energy. Tunable IR radiation was scanned in steps of 2 cm^{-1} while narrowing down to 1 cm^{-1} from 2250 to 2450 cm^{-1} for extracting detailed spectral substructures. The obtained infrared spectra were normalized by the parent ion signal and IR laser energy.

Quantum chemical calculations were performed to determine energetically low-lying structures of target complexes. Genmer[47,48] was used to extensively generate initial guess structures of the studied species. The semiempirical quantum mechanical method GFN2-xTB[49] was employed to pre-optimize complex geometries using the xtb[50] program. The resulting low-energy isomers were reoptimized at the PBE0-D3(BJ)/def2-TZVP level of theory.[51,52] Vibrational frequency analyses at the same density functional level were performed to ensure that all found minima and transition states have zero and only one imaginary frequency, respectively. Intrinsic reaction coordinate (IRC) calculations were carried out to confirm that each reported transition state appropriately links the corresponding reactant and product.[53–56] All the DFT calculations were performed with the Gaussian 16 software package.[57] Simulated IR spectra were derived from the calculated harmonic vibrational frequencies scaled by a factor of 0.957 and further convoluted with Lorentzian functions using 8 or 15 cm^{-1} full width at half-maximum (FWHM) to reproduce spectral features. The scaling factor was determined by comparing the experimental and calculated values of free CO_2 antisymmetric stretching vibrational frequencies.

3. Results and discussion

3.1 Different structural motifs

$Sc_2O_2^+$ cations were produced through pulsed laser ablation of a scandium metal target in the presence of He seeded with CO_2 as the carrier gas. The ground-state electronic structure of $Sc_2O_2^+$ was theoretically determined to be the doublet state, consistent with the previous study.[58] The optimized geometry converged to a planar structure with a Sc–O–Sc angle of 94.8° and two distinct Sc–O bond lengths of 1.82 and 1.88 Å, respectively (Fig. S2, ESI†). Using the distorted rhombus structure with C_{2v} symmetry found for the bare ion, extensive calculations have been conducted to reveal the possible activation of CO_2 molecules by $Sc_2O_2^+$ cation upon complexation. In the search for stable geometries of $[Sc_2O_2(CO_2)_n]^+$ (n = 1–4) ion–molecule complexes, both activated and molecularly adsorbed CO_2 were identified. The reaction products of the $Sc_2O_2^+$ cation with different numbers of CO_2 molecules were
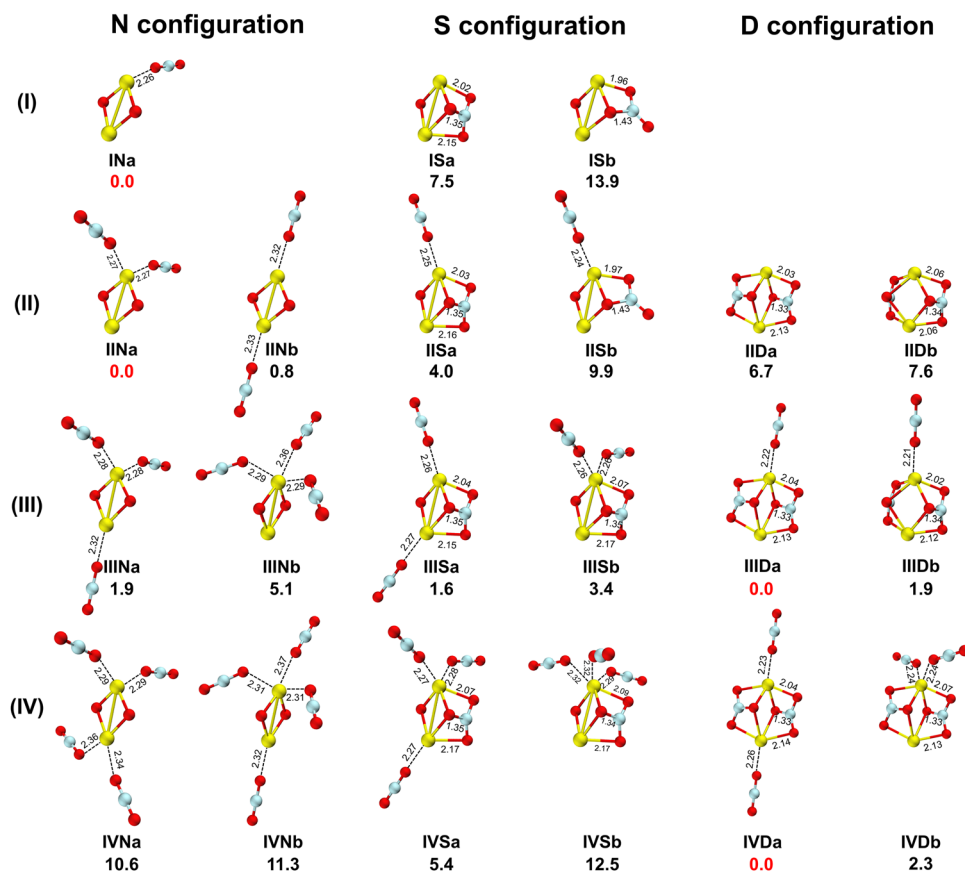
32854 | *Phys. Chem. Chem. Phys.*, 2023, **25**, 32853–32862

This journal is © the Owner Societies 2023

Fig. 1 Low-lying structures of $[Sc_2O_2(CO_2)_n]^+$ (n = 1–4) ion–molecule complexes calculated at the PBE0-D3(BJ)/def2-TZVP level of theory. Relative Gibbs free energies (at 298 K) are given in kcal mol^{-1}. Bond lengths are noted in Å.

grouped according to similar binding motifs, including the end-on-only configuration and two distinct carbonate coordination modes.

Fig. 1 shows energetically low-lying isomers as representatives from each category along with their relative Gibbs free energies in kcal mol^{-1}. The lowest-energy structure found for the n = 1 product is a planar $Sc_2O_2^+$ core ion bound with molecular CO_2 through typical charge–quadrupole interactions[59–61] and is labeled as INa, in which N represents nonactivated forms. The $Sc_2O_2^+$ cation can also react with CO_2 to form a compact structure ISa, which exhibits a novel tridentate binding pattern and lies 7.5 kcal mol^{-1} above the global minimum INa. This unique configuration contains a bent CO_2 moiety in which the C atom binds to an O atom from the $Sc_2O_2^+$ part forming a new covalent C–O bond, while the two O atoms each bind to a Sc atom to form two additional Sc–O bonds. Looking at this structure from an unconventional perspective, ISa can be viewed as a single carbonate group coordinated to a metal oxide center, where S indicates the presence of core structures with one carbonate. This is the first tridentate carbonate-containing adduct found in the model systems involving positively charged metal oxides to the best of our knowledge. A similar bridge tridentate carbonate unit has been reported in the theoretical studies on the reactions of CO_2 with neutral and anionic M_3O_6 (M = Ti and Zr) metal oxides.[45,46] Of

the third isomer ISb with the S coordination mode, the activated CO_2 was predicted to react with a bridging O atom from the metal oxide and bind to a metal atom with one of its oxygen atoms, leading to a bidentate carbonate structure that is higher in energy by 6.4 kcal mol^{-1} compared to ISa.

Two lowest-lying isomers characteristic of molecularly coordinated CO_2 ligands were located for n = 2 complexes, presenting a small energy difference of 0.8 kcal mol^{-1}. In the most stable structure IINa with C_{2v} symmetry, two CO_2 molecules connect to the same Sc atom; while isomer IINb has two distinct Sc···O bonds between each Sc end of the metal oxide center and O atoms from two CO_2 molecules. The complexes with S structural motifs are displayed as isomers IISa and IISb, each featuring a tridentate or bidentate carbonate core structure and can be perceived as ISa and ISb solvated by one CO_2 ligand, respectively. Compared to n = 1 species, there are significantly lower energy differences between the N and S isomers, with IISa and IISb being higher in energy by 4.0 and 9.9 kcal mol^{-1} compared to IINa. Notably, a unique activated form of double carbonate structural motifs was found for larger complexes starting from n = 2 and is categorized into a new group denoted as D configuration. The corresponding low-lying structures, IIDa and IIDb, differ in the relative orientation of two carbonate moieties and lie 6.7 and 7.6 kcal mol^{-1} above the most stable structure, respectively.

This journal is © the Owner Societies 2023

Phys. Chem. Chem. Phys., 2023, **25**, 32853–32862 | **32855**

In contrast to complexes with smaller sizes, the energetically lowest-lying structure calculated for $n = 3$ species is an activated reaction product, IIIDa, where two CO_2 molecules bind with the metal oxide center, forming a double carbonate core structure. Additionally, the energy order of low-lying isomers in three different groups reverses starting from $n = 3$. This change suggests a size-varying scenario in terms of ion population, with larger clusters probably dictated by carbonate-containing structures rather than end-on configurations. As illustrated in Fig. 1, isomers IIIDa and IIIDb can essentially be regarded as IIDa and IIDb, each binding with a third CO_2 molecule through one of Sc atoms. Structures with a single tridentate carbonate, IIISa and IIISb, were identified as being located in regions with considerably lower energy on the potential energy surface compared to analogues with $n = 1$ and 2. Bidentate binding motifs are much less stable than those with tridentate carbonates and accordingly not included for further analysis. Isomers IIINa and IIINb in N series, with all three CO_2 molecules terminally bound to Sc atoms, are higher in energy by 1.9 and 5.1 kcal mol^{-1} compared to IIIDa, respectively.

For $n = 4$ complexes, the D configuration remains the most stable geometry, while the conventional $[Sc_2O_2(CO_2)_n]^+$ type of structure in which all CO_2 ligands bound in a simple η^1-O manner is determined to lie much higher in energy than the carbonate-containing isomers IVSa and IVDa. Isomer IVSa having a single tridentate center is the third lowest-energy structure, 5.4 kcal mol^{-1} less stable than the global minimum geometry IVDa. The fact that carbonate structures are markedly lower in energy than N isomers upon successive CO_2 ligand addition implies a greater possibility of activation in larger complexes.

3.2 Activation mechanisms of CO_2 molecules by $Sc_2O_2^+$ ion centers

With the aim of gaining mechanistic insights into the formation of the carbonate substructure from molecularly bound isomers, it is now of great interest to explore reaction pathways linking all representative structures for different complex sizes. Despite the complexity encountered in determining specific transition states corresponding to CO_2 activation, we have identified a general reaction pathway involving a two-step conversion for tridentate carbonate moiety formation as manifested in Fig. 2. In the first panel shown for $n = 1$ species, the first-step activation of CO_2 starting from the encounter complex INa proceeds with a substantial energy barrier of 17.0 kcal mol^{-1}. The transition state TS1 involves a decrease in the Sc···O bond length, along with the distortion of CO_2 molecules and the formation of a new C–O covalent bond between the C atom of CO_2 and a bridging O atom from metal oxide. An intermediate structure with a bidentate carbonate unit labeled as IM1 (essentially isomer ISb mentioned above) is accessed by overcoming TS1, which connects two saddle points TS1 and TS2 on the potential energy surface. The second barrier associated with a small extent of structural rearrangement is drastically easier to surmount compared to the initial stage. The next Sc–O bond formation between the metal center and
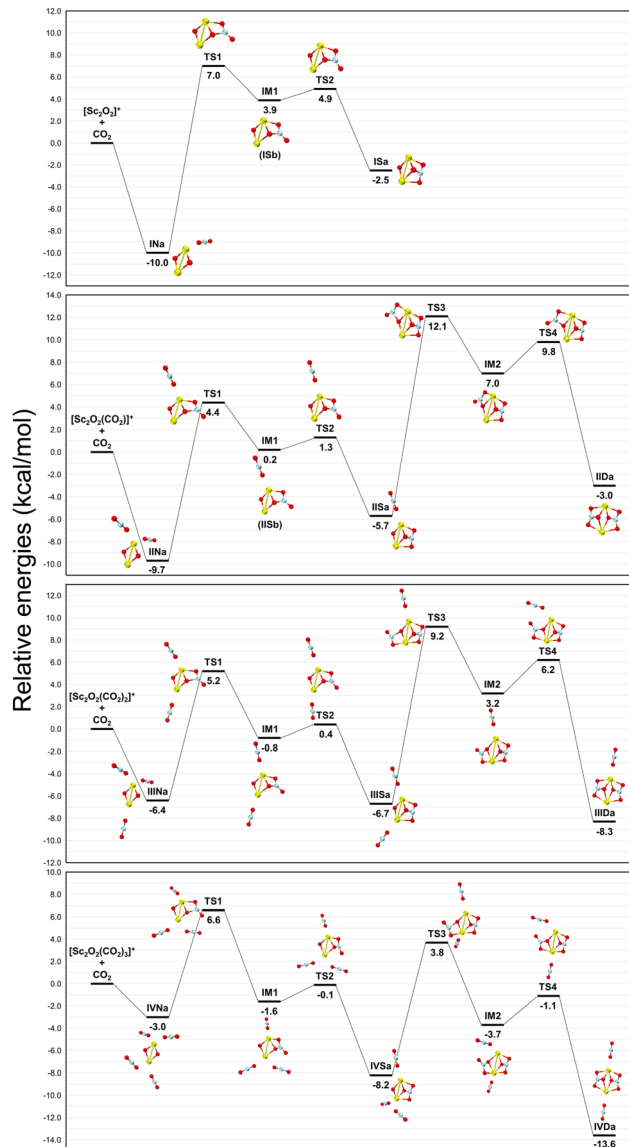

Fig. 2 Reaction pathways for the transformations from N isomers to S and D isomers on the Gibbs free energy surfaces of $[Sc_2O_2(CO_2)_n]^+$ ($n = 1$–4) species calculated at the PBE0-D3(BJ)/def2-TZVP level of theory. Relative Gibbs free energies (at 298 K) are given in kcal mol^{-1}.

the oxygen atom of CO_2 is accomplished by crossing TS2, eventually leading to an energetically unfavorable isomer ISa. This reaction pathway demonstrates a typical transformation process from molecular interactions to a single-carbonate structure with a tridentate binding motif.

The reactions involving more CO_2 molecules feature nearly identical transition state core structures as predicted for $n = 1$ complexes (all denoted as TS1 in Fig. 2). Subsequent bidentate carbonate structures reached as intermediates (IM1) can readily convert into S isomers over small barriers within 1.5 kcal mol^{-1} in a similar fashion. Starting from $n = 2$, an additional CO_2 molecule shows the potential for activation with even higher reaction barrier heights, eventually resulting in D configurations. It should be noted that the reaction barriers calculated
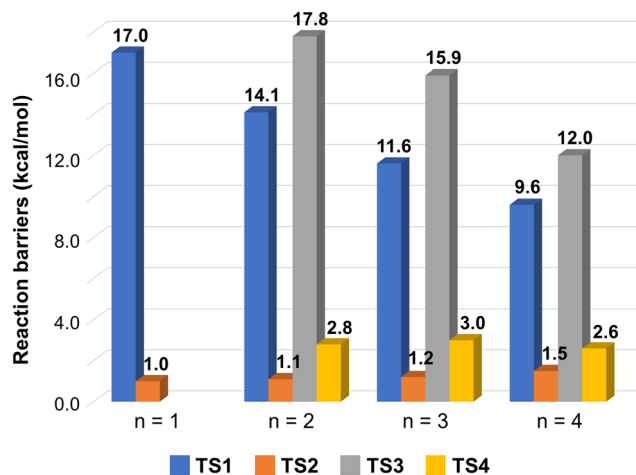
32856 | Phys. Chem. Chem. Phys., 2023, 25, 32853–32862

This journal is © the Owner Societies 2023

Fig. 3 Calculated reaction barrier heights for each step along the trans-formations from N to D isomers on the potential energy surfaces of $[Sc_2O_2(CO_2)_n]^+$ (n = 1–4) species at the PBE0-D3(BJ)/def2-TZVP level of theory. Relative Gibbs free energies (at 298 K) are given in kcal mol^{-1}.

for the first activation step show an evident decreasing trend from 17.0 to 9.6 kcal mol^{-1} with increasing complex size (blue columns in Fig. 3). Moreover, there is also a significant drop in the reaction barriers (from 17.8 to 12.0 kcal mol^{-1}) calculated for the first-stage of the second carbonate moiety formation from S to D isomers. While molecularly bound complexes are likely to be prevalent among smaller complexes from both energy and reaction complexity perspectives, carbonate structures tend to dominate for larger complexes considering remarkably lower energy and conversion barriers. These courses of consecutive reactions can hardly illustrate a complete reaction scenario on the potential energy surfaces for different cluster sizes; however, they allow us to speculate about the possible isomers that could be produced and how the isomeric distributions might be.

One major contributor to the activation barriers is the energy required to deform reactants from their equilibrium geometries on the way to corresponding TSs (Fig. 4A) as reaction proceeds, commonly known as "distortion energy" (see details in ESI†).[62,63] The distortion energy can be naturally divided into two individual participants in this case, *i.e.*, $[Sc_2O_2]$ and $[CO_2]$ as displayed in Fig. 4B. When evaluated as a function of complex size, the distortion energy exhibits the same descending trend as predicted for the reaction barrier (Fig. 4C), demonstrating its principal role in lowering the barrier by alleviating the energy cost related to reactant deformation. A closer inspection of respective distortion energies reveals a consistent higher energy penalty arising from the $[CO_2]$ part, at least three times the strain energy of $[Sc_2O_2]$. Specifically, this distortion energy stems from the deviations of CO_2 molecule from linear geometry to a bent structure, as demonstrated by the bond angle O1–C1–O2 derived from TS1 geometries (from 146.3 to 152.9°, Fig. 4D).

Furthermore, in order to obtain comprehensive information about the size-dependent degrees of distortion, atomic charges

on Sc1 and O3 atoms in all encounter complexes (I–IVNa) were examined to serve as a simple elucidation. As shown in Fig. 4E, the net charges carried by both Sc1 and O3 reduce upon increasing solvation, leading to weakened attractions of the core ion on adjacent CO_2 molecules. Consequently, the transformation barriers resulting from the deformation of CO_2 molecules present a falling trend as mentioned above. A previous study on $[YO(CO_2)_n]^+$ also revealed a preference for carbonate formation in large clusters along with decreasing conversion barriers from the molecularly bound form to the formation of $[CO_3]$ moiety.[34] The more negative charge on the O atom from yttrium metal oxide with more CO_2 coordination facilitates 2+2 cycloaddition nucleophilic attack and is therefore responsible for lower barriers, which is in contrast to the findings of this work. Based on the calculated atomic charge distributions shown in Fig. S3 (ESI†), CO_2 ligands donate electron density to the metal atoms in N configurations, resulting in significantly less positive charges on Sc. Conversely, in S and D isomers with carbonate structures, tridentate-coordinated CO_2 carries negative charge higher than $-0.4e$ through accepting electron density from the metal oxide center. The combined effect of accepting and donating electron density leads to a reduced degree of activation in larger complexes, accounting qualitatively for increasing O1–C1–O2 angles in TS1 structures.

3.3 Infrared photodissociation spectroscopic characterization

To further develop a fundamental understanding of the critical interactions between $Sc_2O_2^+$ core ion and CO_2 molecules, a series of $[Sc_2O_2(CO_2)_n]^+$ (n = 1–4) complex ions were generated by laser ablation (Fig. S4, ESI†) and further subjected to infrared photodissociation spectroscopic characterization. All experimental spectra were obtained by taking CO_2 loss as depletion in the parent ion signal when scanning laser wavelength from 2100 to 2500 cm^{-1}. Fig. 5 shows the experimentally observed spectrum of $[Sc_2O_2(CO_2)]^+$ complex ions, exhibiting a single broad feature centered at 2376 cm^{-1} in the region of CO_2 antisymmetric stretch. This wide spectral band ranging from 2317 to 2425 cm^{-1} largely results from multiple photon absorption processes that are required to dissociate the molecularly bound CO_2 molecule (see binding energies in Fig. 4F). The IR spectrum of the calculated lowest-energy isomer INa reveals a blue shift of 31 cm^{-1} from the frequency of antisymmetric stretch in free CO_2 (2349 cm^{-1}), which stems from typical charge–quadrupole interactions as reported in similar studies[23,37,64] and it provides a reasonable match to the experimental spectrum. This blue shift can also be attributed to the variation of C–O bond lengths in an antisymmetric manner upon attachment. Low-lying carbonate-containing isomers were not included for comparison due to the lack of absorptions in the relevant frequency range. In consideration of the large activation barrier calculated for n = 1 adducts and their substantial difference in energy, the dominant species generated in the experiments should be N isomers as predicted by DFT.

This journal is © the Owner Societies 2023

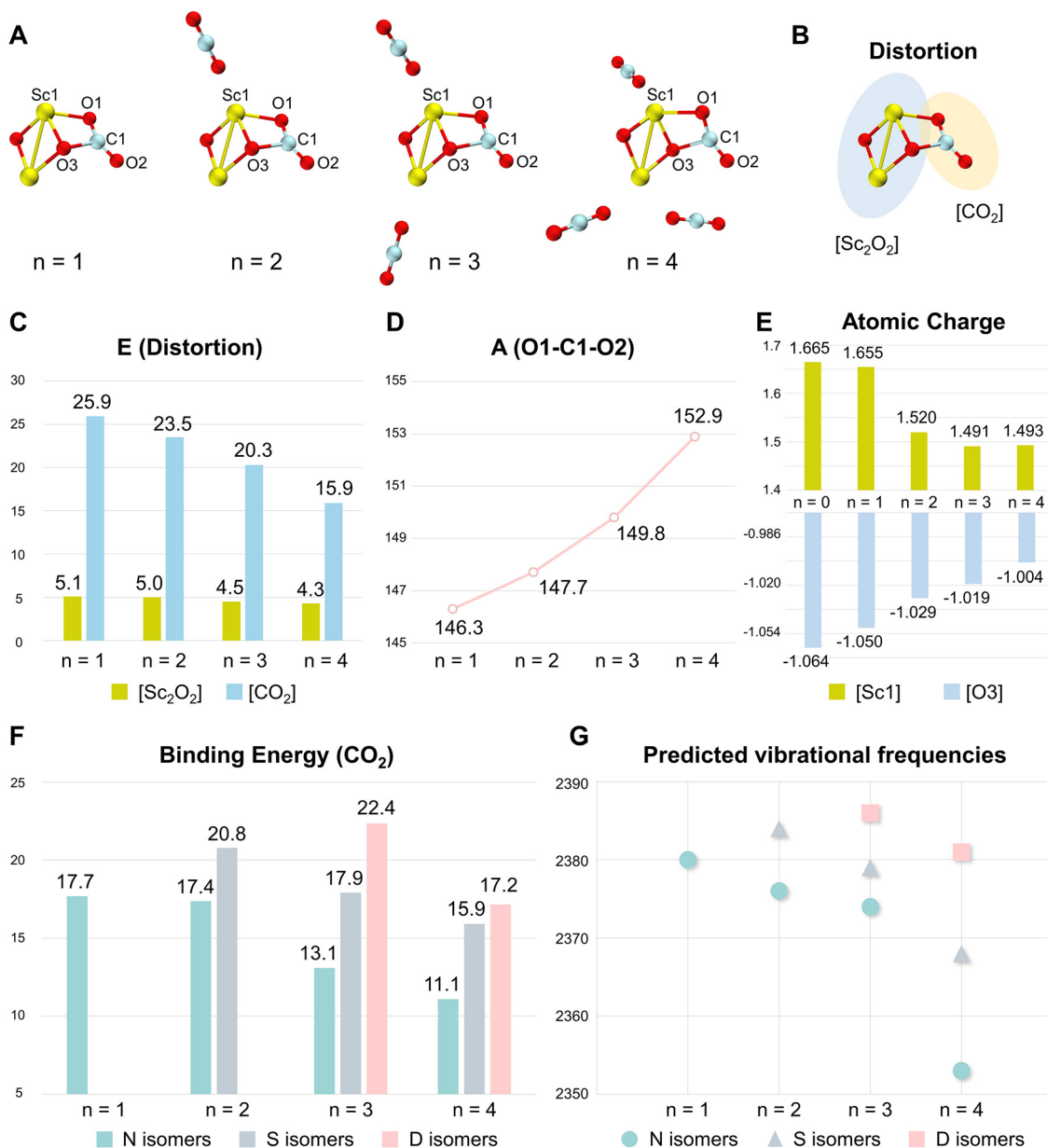*Phys. Chem. Chem. Phys.*, 2023, **25**, 32853–32862 | **32857**

Fig. 4 Theoretical analyses of activation barriers and spectral band assignments. (A) Structures of TS1 for each complex size obtained at the PBE0-D3(BJ)/def2-TZVP level of theory. (B) Separation of the core structure for all TS1s (n = 1–4) into two parts, [Sc_2O_2] and [CO_2]. (C) Distortion energies (in kcal mol^{-1}) of [Sc_2O_2] and [CO_2] parts calculated for all TS1 structures. (D) The O1–C1–O2 bond angles in all TS1 structures. (E) Natural population analysis (NPA) atomic charge distributions of Sc1 and O3 atoms in all lowest-energy N isomers. (F) Binding energies (in kcal mol^{-1}) for the least-tightly bound CO_2 molecules in lowest-energy isomers for all configurations calculated at the PBE0-D3(BJ)/def2-TZVP level of theory. (G) Predicted antisymmetric stretch vibrational frequencies (in cm^{-1}) of the least-tightly bound CO_2 molecules in lowest-energy isomers for all configurations.

The experimental spectrum of the $[Sc_2O_2(CO_2)_2]^+$ complex ion shown in Fig. 6 contains a major peak at 2369 cm^{-1} with a shoulder at 2391 cm^{-1} on the higher energy side. The calculated spectra for low-lying N and S isomers are also displayed for spectral assignments, while intermediate IISb was not taken into consideration due to its effortless conversion to isomer IISa over a small barrier. The IR spectrum of IINb provides the best match for the most prominent spectral feature, corresponding to the out-of-phase combination of antisymmetric stretch vibrations of two CO_2 ligands on each end. Both N

isomers can coexist in experiment considering the insignificant energy difference in isomer stability. Given the lower binding energy of CO_2 in isomer IINb (Table S1, ESI†) and therefore higher dissociation yields, it is plausible that the observed photodissociation spectrum presents the characteristics of IINb rather than the lowest-energy isomer. However, the presence of isomer IINa should not be disregarded considering the unresolved spectral feature between the main peak and the small band at 2391 cm^{-1}. The remaining weaker absorption band is attributed to the antisymmetric stretch of a more tightly bound
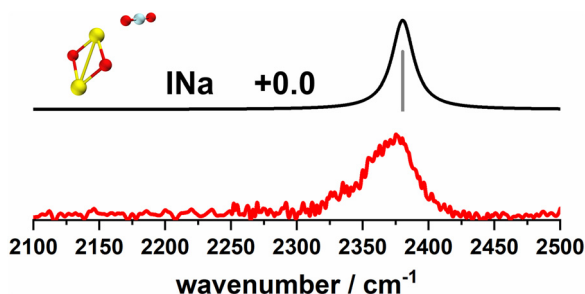
32858 | Phys. Chem. Chem. Phys., 2023, 25, 32853–32862

This journal is © the Owner Societies 2023

Fig. 5 Experimental IRPD spectrum of the $[Sc_2O_2(CO_2)]^+$ ion–molecule complex together with the simulated IR spectrum for isomer INa in the spectral region of 2100–2500 cm^{-1}.

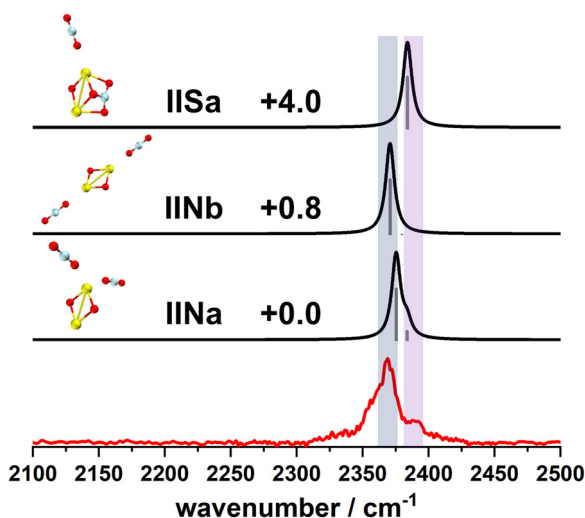Fig. 6 Experimental IRPD spectrum of the $[Sc_2O_2(CO_2)_2]^+$ ion–molecule complex together with the simulated IR spectra for three low-lying isomers in the spectral region of 2100–2500 cm^{-1}.

Fig. 7 Experimental IRPD spectrum of the $[Sc_2O_2(CO_2)_3]^+$ ion–molecule complex together with the simulated IR spectra for six low-lying isomers in the spectral region of 2100–2500 cm^{-1}.

CO_2 molecule, as the frequency is significantly blue-shifted from that of free CO_2. The predicted spectrum of IISa shows an acceptable agreement with the low-intensity feature, providing clues for the presence of carbonate-containing structures.

For complexes with three CO_2 molecules, the experimental spectrum (Fig. 7) exhibits a similar doublet feature as in the $[Sc_2O_2(CO_2)_2]^+$ complex, including the absorption maximum at 2364 cm^{-1} and a sideband at 2384 cm^{-1}. Based on the comparison between the experimental and simulated spectra for all low-lying isomers with distinct configurations, the strong absorption is assigned to an N isomer, IIINb, which is less stable than IIIDa by 5.1 kcal mol^{-1}. The similar finding that the observed feature in the low-frequency region is matched by a high-lying N isomer can also be explained by a loosely bound CO_2 ligand with lower binding energy in IIINb (Table S1, ESI†). Upon closer examination of the relative intensity and the band gap between two experimental peaks, it becomes apparent that the weaker band lying higher than 2375 cm^{-1} cannot be solely attributed to the presence of N isomers. Combined with the relative energies and significantly lower conversion barriers
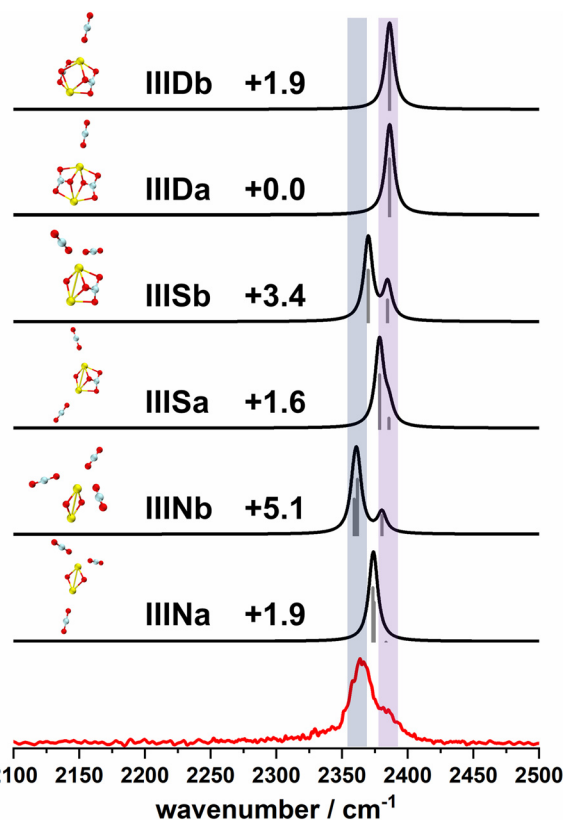
at n = 3, carbonate structures should be taken into account to interpret this two partially resolved peaks. Furthermore, the increasing intensity of the band in the blue region may suggest a higher population of energetically more favorable carbonate structures compared to n = 2 complexes. However, it is difficult to distinguish the principal contributors in the higher-energy region due to the overlapping IR signatures predicted for carbonate structures.

The experimental spectrum of the $[Sc_2O_2(CO_2)_4]^+$ complex ion shown in Fig. 8 presents an unresolved broad band ranging from 2332 to 2414 cm^{-1}. The intense absorption around 2356 cm^{-1} is attributed to a weakly coordinated CO_2 molecule in isomer IVNa based on the same reason proposed for complexes with smaller sizes, as lower binding energy of CO_2 results in higher photodissociation yields (Fig. 4F). However, the N isomer is unlikely to be the dominant configuration due to its significantly higher energy than carbonate ones and the absence of predicted spectral signals in the high-frequency range. The relatively weaker features in the experimental spectrum can be satisfactorily reproduced by S and D isomers which are both characteristics of IR signatures in the 2375–2400 cm^{-1} region, demonstrating the formation of $[CO_3]$ units bound to scandium oxide *via* a tridentate motif.

Inspection of the IR spectra calculated for all representative isomers shows obvious deviations in the frequencies of
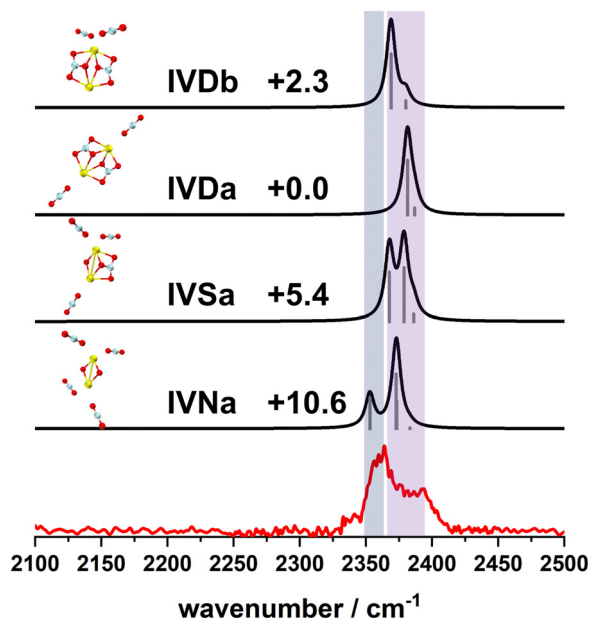
This journal is © the Owner Societies 2023

Phys. Chem. Chem. Phys., 2023, **25**, 32853–32862 | **32859**

Fig. 8 Experimental IRPD spectrum of the $[Sc_2O_2(CO_2)_4]^+$ ion–molecule complex together with the simulated IR spectra for four low-lying isomers in the spectral region of 2100–2500 cm^{-1}.

antisymmetric stretching mode of the least-tightly bound CO_2 molecule. As summarized in Fig. 4G, corresponding frequencies of N isomers persist to be less blue-shifted from that of free CO_2 than S and D isomers among all sizes, in particular for $n = 4$. The reason for such discrepancies between non-carbonate and carbonate structures is due to substantial variations in the binding energies of end-on CO_2 molecules in each configuration (Fig. 4F). D isomers are found to confine CO_2 ligands with the greatest strength, followed by S and N geometries, consistent with predicted spectral features in distinct frequency ranges. Consequently, the observation of high-energy bands above *ca.* 2375 cm^{-1} can be deemed as possible evidence of carbonate structure formation under present experimental conditions since $n = 2$. The weaker intensity of these bands can also be expected, given the large calculated reaction barriers above the entrance channel for the formation of carbonate units along with their higher dissociation energy. In addition, the rising relative intensity of the small spectral signals with increasing CO_2 numbers is in line with increasing stability of carbonate structures, as well as reducing CO_2 binding energies and accordingly higher dissociation yields.

4. Conclusions

In this work, we have explored the gas-phase reactions of $Sc_2O_2^+$ with different numbers of CO_2 molecules using infrared photodissociation spectroscopy combined with quantum chemical calculations. Two structural motifs of $[Sc_2O_2(CO_2)_n]^+$ ion–molecule complexes are predicted using DFT and can be summarized into end-on-only and carbonate-containing configuration. The latter becomes the most stable geometry with increasing complex sizes. The computation results indicate that

molecularly bound CO_2 is able to bind with the $Sc_2O_2^+$ ion center in a tridentate fashion resulting in the formation of a carbonate moiety through a two-step structural rearrangement involving substantial energy barriers, where the electron density donation from the metal oxide center is found to be responsible for CO_2 activation. Assignment of the spectral bands in the higher energy range suggests the formation of carbonate structures from $n = 2$, albeit with large calculated reaction barriers hindering the activation. Increasing the extent of solvation significantly lowers the distortion energies associated with approaching transition states, leading to less prohibitive barrier heights on the path to carbonate formation. The present results provide valuable insights into the activation mechanisms of $Sc_2O_2^+$ towards CO_2 molecules and propose new directions in the quest for the rational design of transition metal oxide catalysts in the field of CO_2 utilization.

Author contributions

P. L., conceptualization, formal analysis, investigation and writing – original draft. J. H., formal analysis, investigation and writing – original draft. Y. C., S. L. and Q. S., investigation and methodology. X. Z. and W. Z., supervision, writing – review and editing and funding acquisition.

Conflicts of interest

The authors declare no conflict of interest.

Acknowledgements

References

1 T. A. Jacobson, J. S. Kler, M. T. Hernke, R. K. Braun, K. C. Meyer and W. E. Funk, *Nat. Sustainability*, 2019, **2**, 691–701.

2 L. Cao, G. Bala, K. Caldeira, R. Nemani and G. Ban-Weiss, *Proc. Natl. Acad. Sci. U. S. A.*, 2010, **107**, 9513–9518.

3 P. M. Visser, J. M. H. Verspagen, G. Sandrini, L. J. Stal, H. C. P. Matthijs, T. W. Davis, H. W. Paerl and J. Huisman, *Harmful Algae*, 2016, **54**, 145–159.

4 H. d Coninck and S. M. Benson, *Annu. Rev. Environ. Resour.*, 2014, **39**, 243–270.

5 T. M. Gür, *Prog. Energy Combust. Sci.*, 2022, **89**, 100965.

6 D. M. D'Alessandro, B. Smit and J. R. Long, *Angew. Chem., Int. Ed.*, 2010, **49**, 6058–6082.

32860 | *Phys. Chem. Chem. Phys.*, 2023, **25**, 32853–32862

This journal is © the Owner Societies 2023

7 W. Gao, S. Liang, R. Wang, Q. Jiang, Y. Zhang, Q. Zheng, B. Xie, C. Y. Toe, X. Zhu and J. Wang, *et al.*, *Chem. Soc. Rev.*, 2020, **49**, 8584–8686.

8 M. Mikkelsen, M. Jørgensen and F. C. Krebs, *Energy Environ. Sci.*, 2010, **3**, 43–81.

9 M. Peters, B. Köhler, W. Kuckshinrichs, W. Leitner, P. Markewitz and T. E. Müller, *ChemSusChem*, 2011, **4**, 1216–1240.

10 Q. Liu, L. Wu, R. Jackstell and M. Beller, *Nat. Commun.*, 2015, **6**, 5933.

11 S. C. Peter, *ACS Energy Lett.*, 2018, **3**, 1557–1561.

12 L. G. Dodson, M. C. Thompson and J. M. Weber, *Annu. Rev. Phys. Chem.*, 2018, **69**, 231–252.

13 R. Wang, G. Liu, S. K. Kim, K. H. Bowen and X. Zhang, *J. Energy Chem.*, 2021, **63**, 130–137.

14 M. Nolan and M. Fronzi, *Catal. Today*, 2019, **326**, 68–74.

15 J. Wu, Y. Huang, W. Ye and Y. Li, *Adv. Sci.*, 2017, **4**, 1700194.

16 K. Li, X. An, K. H. Park, M. Khraisheh and J. Tang, *Catal. Today*, 2014, **224**, 3–12.

17 M. Marszewski, S. Cao, J. Yu and M. Jaroniec, *Mater. Horiz.*, 2015, **2**, 261–278.

18 E. Tayyebi, J. Hussain, Y. Abghoui and E. Skúlason, *J. Phys. Chem. C*, 2018, **122**, 10078–10087.

19 W. Jiang, H. Loh, B. Q. L. Low, H. Zhu, J. Low, J. Z. X. Heng, K. Y. Tang, Z. Li, X. J. Loh and E. Ye, *et al.*, *Appl. Catal., B*, 2023, **321**, 122079.

20 S. N. Habisreutinger, L. Schmidt-Mende and J. K. Stolarczyk, *Angew. Chem., Int. Ed.*, 2013, **52**, 7372–7408.

21 J. Ran, M. Jaroniec and S.-Z. Qiao, *Adv. Mater.*, 2018, **30**, 1704649.

22 U. Burghaus, *Prog. Surf. Sci.*, 2014, **89**, 161–217.

23 A. M. Ricks, A. D. Brathwaite and M. A. Duncan, *J. Phys. Chem. A*, 2013, **117**, 11490–11498.

24 M. C. Thompson, J. Ramsay and J. M. Weber, *Angew. Chem., Int. Ed.*, 2016, **55**, 15171–15174.

25 S. Zhou, J. Li, M. Firouzbakht, M. Schlangen and H. Schwarz, *J. Am. Chem. Soc.*, 2017, **139**, 6169–6176.

26 Y. Yang, Y.-K. Li, Y.-X. Zhao, G.-P. Wei, Y. Ren, K. R. Asmis and S.-G. He, *Angew. Chem., Int. Ed.*, 2021, **60**, 13788–13792.

27 J. Jin, S. Pan, X. Jin, S. Lei, L. Zhao, G. Frenking and M. Zhou, *Chem. – Eur. J.*, 2019, **25**, 3229–3234.

28 X. Dong, L. Wang, G. Wang and M. Zhou, *J. Phys. Chem. A*, 2022, **126**, 4598–4607.

29 X. Kong, R. Shi, C. Wang, H. Zheng, T. Wang, X. Liang, J. Yang, Q. Jing, Y. Liu and H. Han, *et al.*, *Chem. Phys.*, 2020, **534**, 110755.

30 W. Cao, Z. Hu, X. Peng, H. Sun, Z. Sun and X.-B. Wang, *J. Am. Chem. Soc.*, 2022, **144**, 19317–19325.

31 X. Cao, M. Chen, J. Ma, B. Yin and X. Xing, *Phys. Chem. Chem. Phys.*, 2017, **19**, 196–203.

32 N. R. Walker, G. A. Grieves, R. S. Walters and M. A. Duncan, *Chem. Phys. Lett.*, 2003, **380**, 230–236.

33 N. Zimmermann, T. M. Bernhardt, J. M. Bakker, R. N. Barnett, U. Landman and S. M. Lang, *J. Phys. Chem. A*, 2020, **124**, 1561–1566.

34 Z. Zhao, X. Kong, Q. Yuan, H. Xie, D. Yang, J. Zhao, H. Fan and L. Jiang, *Phys. Chem. Chem. Phys.*, 2018, **20**, 19314–19320.

35 D. Yang, M.-Z. Su, H.-J. Zheng, Z. Zhao, X.-T. Kong, G. Li, H. Xie, W.-Q. Zhang, H.-J. Fan and L. Jiang, *Chin. J. Chem. Phys.*, 2020, **33**, 160–166.

36 A. Iskra, A. S. Gentleman, E. M. Cunningham and S. R. Mackenzie, *Int. J. Mass Spectrom.*, 2019, **435**, 93–100.

37 E. I. Brewer, A. E. Green, A. S. Gentleman, P. W. Beardsmore, P. A. J. Pearcy, G. Meizyte, J. Pickering and S. R. Mackenzie, *Phys. Chem. Chem. Phys.*, 2022, **24**, 22716–22723.

38 J. Han, Y. Yang, B. Qiu, P. Liu, X. Wu, G. Wang, S. Liu and X. Zhou, *Phys. Chem. Chem. Phys.*, 2023, **25**, 13198–13208.

39 H. Zheng, X. Kong, C. Wang, T. Wang, D. Yang, G. Li, H. Xie, Z. Zhao, R. Shi and H. Han, *et al.*, *J. Phys. Chem. Lett.*, 2021, **12**, 472–477.

40 M. Salzburger, R. T. Saragi, F. J. Wensink, E. M. Cunningham, M. K. Beyer, J. M. Bakker, M. Ončák and C. van der Linde, *J. Phys. Chem. A*, 2023, **127**, 3402–3411.

41 B. J. Knurr and J. M. Weber, *J. Phys. Chem. A*, 2015, **119**, 843–850.

42 L. G. Dodson, M. C. Thompson and J. M. Weber, *J. Phys. Chem. A*, 2018, **122**, 6909–6917.

43 S. Debnath, X. Song, M. R. Fagiani, M. L. Weichman, M. Gao, S. Maeda, T. Taketsugu, W. Schöllkopf, A. Lyalin and D. M. Neumark, *et al.*, *J. Phys. Chem. C*, 2019, **123**, 8439–8446.

44 S. Debnath, X. Song, M. R. Fagiani, M. L. Weichman, M. Gao, S. Maeda, T. Taketsugu, W. Schöllkopf, A. Lyalin and D. M. Neumark, *et al.*, *J. Phys. Chem. C*, 2020, **124**, 6952–6953.

45 L. A. Flores, J. G. Murphy, W. B. Copeland and D. A. Dixon, *J. Phys. Chem. A*, 2017, **121**, 8719–8727.

46 Y. Hu, R. R. Persaud, M. Vasiliu and D. A. Dixon, *J. Phys. Chem. A*, 2020, **124**, 5402–5407.

47 T. Lu and F. Chen, *J. Comput. Chem.*, 2012, **33**, 580–592.

48 T. Lu, *Molclus Program*, 1.9.9.3, 2021, **https://www.keinsci.com/research/molclus.html**, (accessed July 8 2021).

49 C. Bannwarth, S. Ehlert and S. Grimme, *J. Chem. Theory Comput.*, 2019, **15**, 1652–1671.

50 S. Grimme, C. Bannwarth and P. Shushkov, *J. Chem. Theory Comput.*, 2017, **13**, 1989–2009.

51 C. Adamo and V. Barone, *J. Chem. Phys.*, 1999, **110**, 6158–6170.

52 S. Grimme, S. Ehrlich and L. Goerigk, *J. Comput. Chem.*, 2011, **32**, 1456–1465.

53 K. Fukui, *J. Phys. Chem.*, 1970, **74**, 4161–4163.

54 K. Fukui, *Acc. Chem. Res.*, 1981, **14**, 363–368.

55 C. Gonzalez and H. B. Schlegel, *J. Phys. Chem.*, 1990, **94**, 5523–5527.

56 D. G. Truhlar and M. S. Gordon, *Science*, 1990, **249**, 491–498.

57 M. J. Frisch, G. W. Trucks, H. B. Schlegel, G. E. Scuseria, M. A. Robb, J. R. Cheeseman, G. Scalmani, V. Barone, G. A. Petersson, H. Nakatsuji, *et al.*, *Gaussian 16 Rev. C.01*, Wallingford, CT, 2016.

58 L. Wu, C. Zhang, S. A. Krasnokutski and D.-S. Yang, *J. Chem. Phys.*, 2014, **140**, 224307.

This journal is © the Owner Societies 2023

Phys. Chem. Chem. Phys., 2023, **25**, 32853–32862 | **32861**

59 R. S. Walters, N. R. Brinkmann, H. F. Schaefer and M. A. Duncan, *J. Phys. Chem. A*, 2003, **107**, 7396–7405.

60 A. Iskra, A. S. Gentleman, A. Kartouzian, M. J. Kent, A. P. Sharp and S. R. Mackenzie, *J. Phys. Chem. A*, 2017, **121**, 133–140.

61 D. Yang, X. Kong, H. Zheng, M. Su, Z. Zhao, H. Xie, H. Fan, W. Zhang and L. Jiang, *J. Phys. Chem. A*, 2019, **123**, 3703–3708.

62 F. M. Bickelhaupt and K. N. Houk, *Angew. Chem., Int. Ed.*, 2017, **56**, 10070–10086.

63 P. Vermeeren, S. C. C. van der Lubbe, C. Fonseca Guerra, F. M. Bickelhaupt and T. A. Hamlin, *Nat. Protoc.*, 2020, **15**, 649–667.

64 G. Gregoire and M. A. Duncan, *J. Chem. Phys.*, 2002, **117**, 2120–2130.